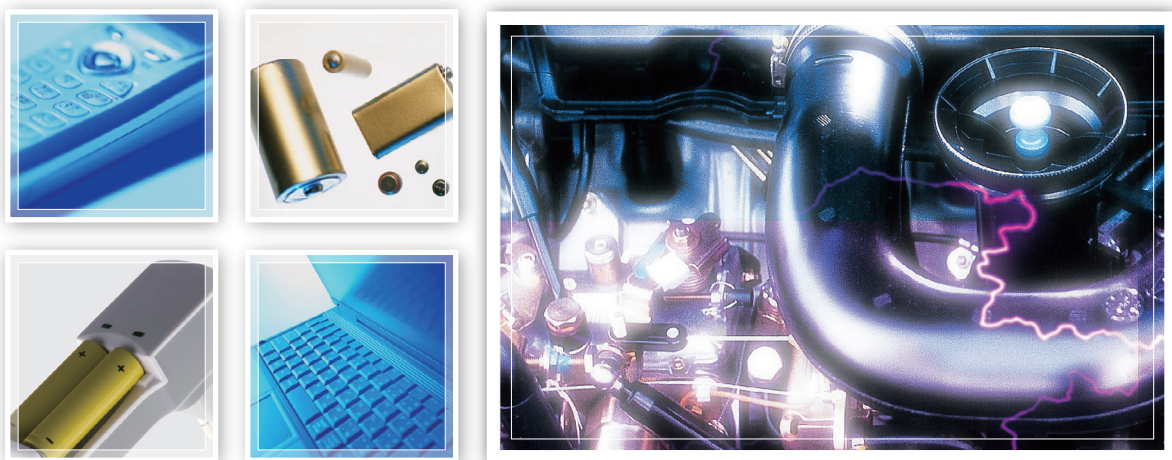


Analytical and Measuring Instruments for Rechargeable Lithium-ion Batteries

Rechargeable Lithium-Ion Battery Evaluation

— APPLICATION NOTEBOOK —



Title	Method	Page
Investigation of Thermal Properties of Lithium-Ion Battery Components	Thermal Analysis	4
Carbon Measurement of Metal Powder Battery Material	Total Organic Carbon Analysis	6
Visualization of the Additive Layer in Vicinity of Negative Electrode in Electrolyte Using SPM-8100FM and Electrochemical Solution Cell in Secondary Batteries	Surface Observation	8
An Examination of the Effects of High/Low Column Cooling Rates Using Nexis GC-2030	Gas Chromatography	10
High-Sensitivity Simultaneous Analysis of Inorganic Gases and Light Hydrocarbons Using Nexis GC-2030 Dual BID System	Gas Chromatography	12
Trace Impurity Analysis of Hydrogen Fuel in Fuel Cell Vehicle-Related Fields	Gas Chromatography	14
Confirmation of Synthesis of Organic Functional Materials Using Benchtop MALDI-TOF MS	MALDI-TOF Mass Spectrometry	16
Investigating the surface and interface of Li ion thin-film battery materials	X-ray Photoelectron Spectroscopy	18
Distribution, segregation and chemical state identification of Lithium salts on Cu electrodes	X-ray Photoelectron Spectroscopy	20



Differential Scanning Calorimeter
DSC-60 Plus



Total Organic Carbon Analyzer
TOC-L



Gas Chromatograph
Nexis GC-2030



Matrix-Assisted
Laser Desorption/Ionization Time-of-Flight Mass Spectrometer
MALDI-8020

Lithium-ion Rechargeable Battery Testing Instrument Matrix

Part	Material	Commonly Used Components	Test Items (Instrument)
Positive electrode	Active material	LiCoO ₂ (lithium cobalt oxide) Mn or Ni may be used instead of Co.	Composition (ICP, XRF) Crystallinity (XRD) Particle size (particle size analyzers) Electron state (XPS)
	Binder	Vinylidene fluoride (polyvinylidene fluoride (PVDF))	Molecular weight distribution (GPC) Surface status (SPM)
	Conduction enhancer	Carbon (carbon black, acetylene black, graphite, etc.)	Composition (FTIR) Crystallinity (XRD)
Negative electrode	Active material	Carbon, graphite	Crystallinity (XRD)
	Trace additive	Li, P, Cu, Na, Co, Ca, K, etc.	Particle size (particle size analyzers) Composition (ICP)
	Binder	SBR (styrene-butadiene rubber) CMC (carboxymethylcellulose), PVDF also used previously	Structure (FTIR)
Separator		Polyolefins (high-density polyethylene)	Structure (FTIR) Thermal characteristics (TG)
Electrolyte solution	Solvent	Carbonate ester, carboxylate ester, ether	Composition (GCMS, GC)
	Electrolyte	LiPF ₆ , LiBF ₄	Composition (ICP)
	Additive	Vinylene carbonate	Composition (GCMS)
Cells Single-cell, module			Compression strength (universal testing machine) Nail penetration testing (materials testing machine) Internal observations (X-ray CT system)

Investigation of Thermal Properties of Lithium-Ion Battery Components

■ Introduction

Lithium-ion batteries are used widely in household electrical appliances such as cell phones and laptop computers. A considerable increase in demand for lithium-ion batteries is predicted in the transportation sector, where they will be used in aeroplanes, hybrid vehicles, and electric vehicles. These applications will require an increase in the power density, efficiency, lifespan, and stability of these batteries. Lithium-ion batteries are composed of a number of parts, including a cathode, anode, electrolyte, and separator. Increasing the performance of lithium-ion batteries will require detailed investigation and analysis of the properties of each of these components, and of the battery as a whole, by instrument analysis. We describe an example investigation of the thermal properties of a lithium-ion battery by thermal analysis.

■ Investigation of Thermal Stability of Electrode Materials

Lithium-ion batteries have a risk of abnormal heat generation or fire from overcharge or from other causes. An investigation of the stability of the battery requires that the behavior of each component be evaluated during heating. The top line in Fig. 1 shows measurements obtained from the cathode active material (LiCoO_4) and electrolyte of a battery after charging using a differential scanning calorimeter. Charging causes the active material to become unstable, and from around 200 °C large exothermic peaks caused by degradation can be seen. This information is important for the selection and preparation of electrode materials since reducing these peaks shows components are more thermally stable and safer at higher temperatures.

The bottom line shows measurements obtained from the cathode active material and electrolyte of a battery before charging. The results show no major heat generation since the active material is stable before charging.

■ Measurement of Moisture Content in Electrode Materials

Lithium-ion batteries are sensitive to moisture and the moisture content of components must be controlled during manufacture. We describe using thermogravimetric analysis (TGA) to calculate the moisture content of LiFePO_4 and graphite electrode active materials.

The graph in Fig. 2 shows temperature on the horizontal axis and percentage weight loss on the vertical axis. Heating the samples and calculating weight loss up to 200 °C showed a small weight change of 0.033 % in the graphite. TGA is normally performed with several tens of milligrams of sample at most, but even smaller changes in weight can be detected by using macro-type thermogravimetric analyzers able to accommodate sample masses in the order of grams.

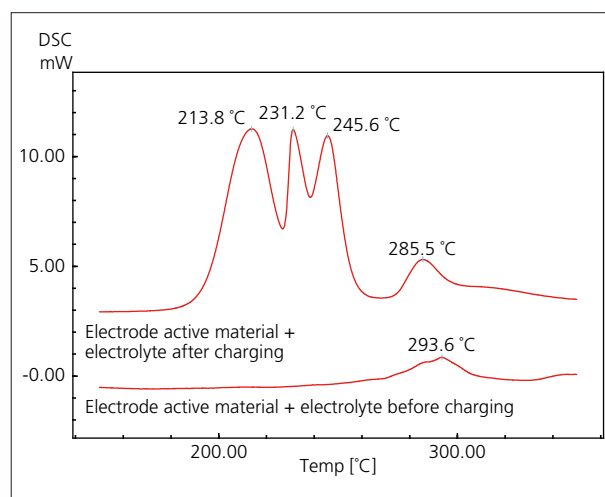


Fig. 1 Differential Scanning Calorimetry (DSC) Measurements of Electrode Active Material and Electrolyte

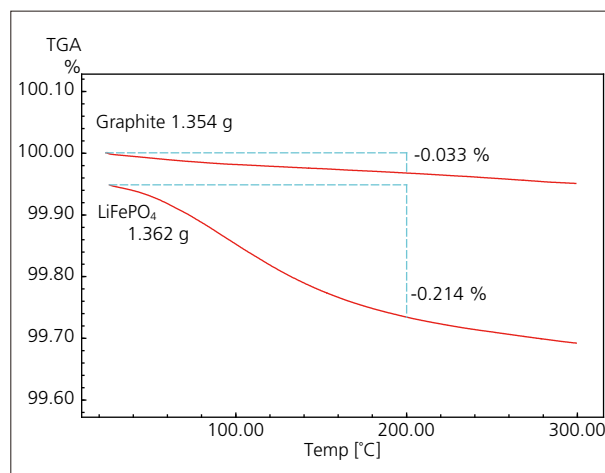


Fig. 2 TGA of Electrode Active Materials

Thermal Properties of Separator

The separator not only prevents short circuit of the cathode and anode but also allows passage of lithium ions and is an important component in terms of battery performance and safety. DSC measurements performed on three different separators are shown in Fig. 3.

Endothermic peaks were recorded for each separator that were probably caused by fusion (melting) of polyethylene in the region of 100 to 150 °C. Melting peak temperatures arose in the order of sample 1, 2, and 3 from lowest to highest temperature.

The separator probably shrinks when it is close to its melting temperature, and we predict that during abnormal heat generation it is safer that shrinking occurs at higher temperatures. A very minor endothermic peak can also be seen around 160 °C for sample 2, which is presumed to be caused by a very small amount of polypropylene in the separator.

Changes in separator dimensions caused by heat and measured by thermo-mechanical analysis (TMA) are shown in Fig. 4. TMA was used to measure extension and shrinking of the separator film while applying a negligible load in a tensile direction. The samples used were the same samples 1 and 2 measured previously with a differential scanning calorimeter, and measurements were taken from each sample in a machine direction (MD) and transverse direction (TD). Comparing the results from each sample, shrinking in both the MD and TD was observed at a higher temperature in sample 2, which corresponds to the results obtained by DSC. There was also less shrinking in the TD compared to the MD in both samples, and TD shrinking was smaller in sample 1 compared to sample 2. Considering safety from the perspective of short circuit prevention during abnormal heat generation, sample 1 is predicted to be less useful because it shrinks at a lower temperature, but also advantageous since it exhibits less TD shrinking.

The results of TMA of stress during shrinking are shown in Fig. 5. Shrink stress increases with increasing temperature, reaches a maximum at around 130 °C, after which it reduces.

These results also show the shrink stress is greater in the MD than TD. Although Fig. 4 shows almost no difference in dimensional changes during shrinking in the MD between samples 1 and 2, a noticeable difference between the samples is apparent in the MD in terms of shrink stress.

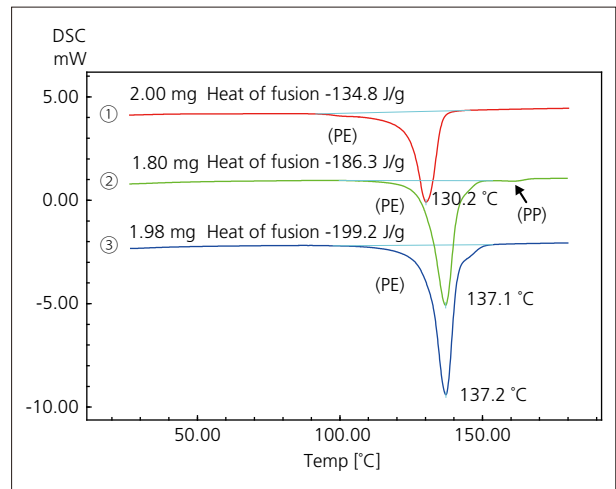


Fig. 3 DSC Measurement of Separators

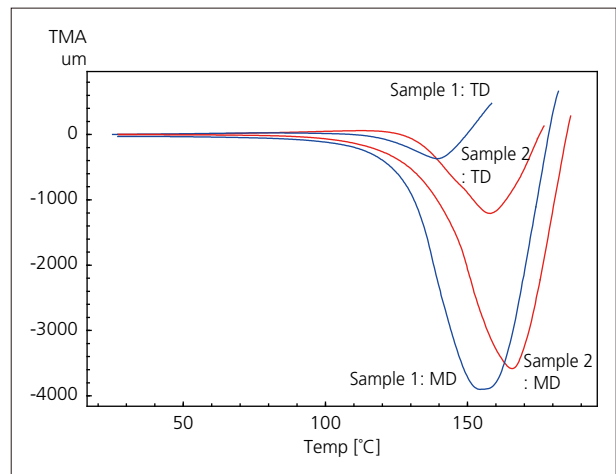


Fig. 4 TMA of Separators

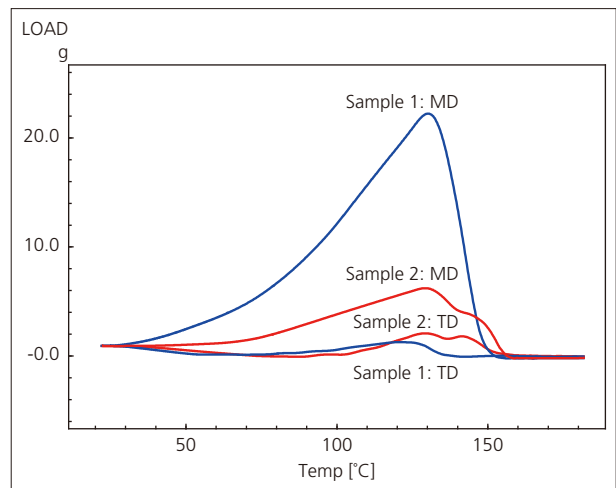


Fig. 5 TMA of Separators (Shrink Stress)

Carbon Measurement of Metal Powder Battery Material

Various metal powders are used in battery electrode materials, depending on the type. Because batteries are used in large quantities in familiar products such as mobile phones, notebook computers, and automobiles, a high level of safety is necessary. Therefore, high purity is demanded in the metal materials used as materials.

Quick, simple measurement of the concentration of carbon contained in metal powders is possible by using a Shimadzu total organic carbon (TOC) solid sample system.

This article introduces an example of total carbon measurement of lithium cobalt oxide, which is widely used as a positive electrode material in lithium ion batteries, by using Shimadzu solid sample system consisting of a TOC-L_{CPH} total organic carbon analyzer and SSM-5000A solid sample combustion unit.

M. Tanaka

■ Analysis Method

Approximately 100 mg of a commercial lithium cobalt oxide (Fig. 2) powder reagent was placed in the sample boat of the SSM-5000A and weighed, and total carbon (TC) was measured. Next, analysis samples were prepared by adding glucose as a carbonaceous substance to 100 mg to 200 mg of lithium cobalt oxide so as to obtain carbon concentrations of 5.0 %, 1.0 %, and 0.2 %, and the TC of the samples was measured.

For calibration of the analyzer, a calibration curve was prepared by TC measurement of a glucose powder reagent (carbon concentration: 40 %).



Fig. 1 Lithium Ion Battery



Fig. 2 Lithium Cobalt Oxide

Table 1 Measurement Conditions

Analyzer	: TOC solid sample system (TOC-L _{CPH} TOC analyzer + SSM-5000A solid sample combustion unit)
Cell length	: Short cell
TC oxidation method	: Combustion catalytic oxidation (Combustion temperature: 900 °C)
Measurement item	: TC (Total carbon)
Calibration curve	: One point calibration curve by glucose powder reagent (Carbon concentration: 40 %)
Sample	: Lithium cobalt oxide (Lithium cobalt (III) oxide, LiCoO ₂) reagent
Additives	: 5 % addition, glucose powder; 1 % addition, 5 %C glucose solution; 0.2 % addition, 0.5 %C glucose solution

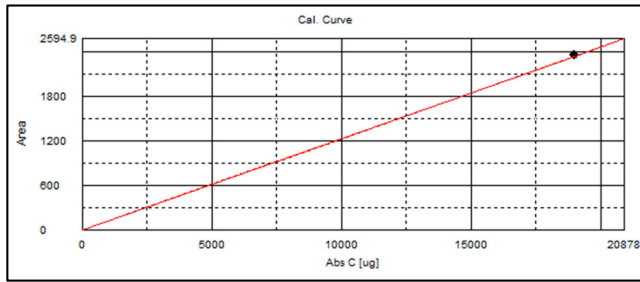
■ Analysis Results

Table 2 shows the results of measurements of the lithium cobalt oxide and the samples with the added carbonaceous substance. Fig. 3 shows the measurement charts. It can be understood that the samples with the added carbonaceous substance were measured with high accuracy.

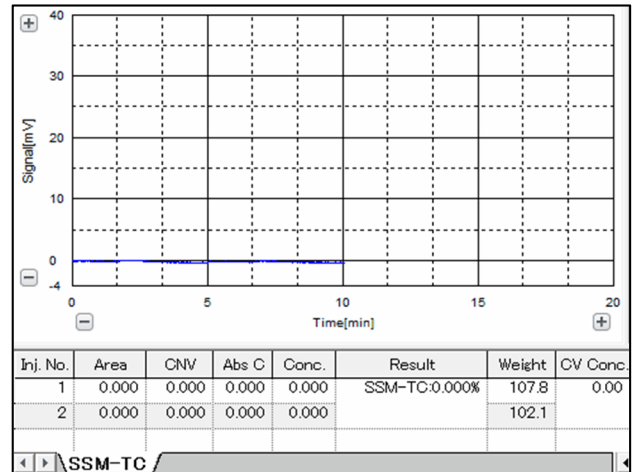
Table 2 Measurement Results

Sample	TC Measurement Value (%C)
Lithium Cobalt Oxide	0
Lithium Cobalt Oxide + 0.2 % Glucose	0.209
Lithium Cobalt Oxide + 1.0 % Glucose	0.999
Lithium Cobalt Oxide + 5.0 % Glucose	5.02

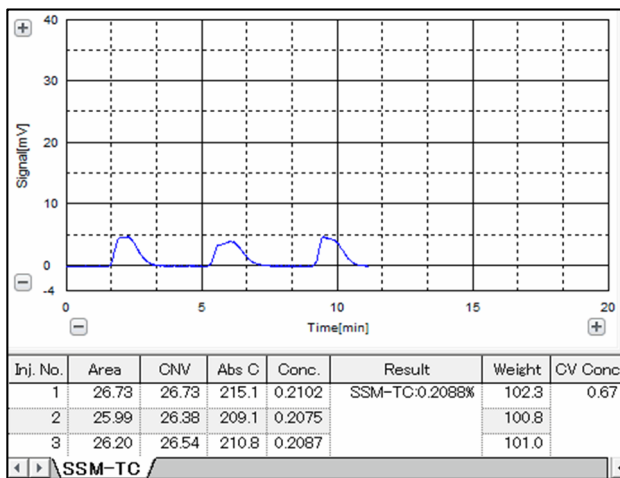
Analysis Data



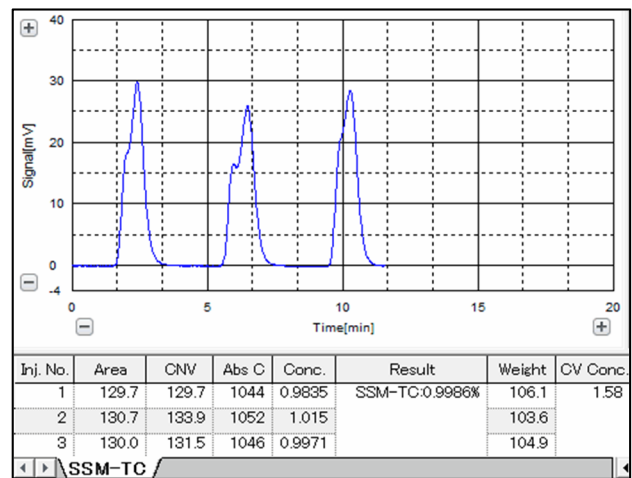
Calibration Curve



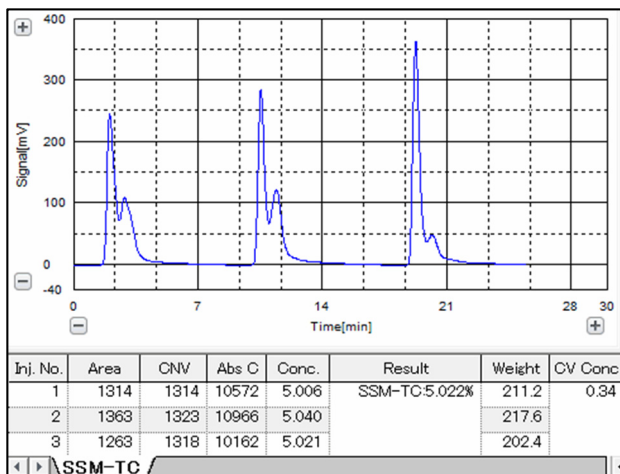
Sample: Lithium Cobalt Oxide



Sample: Lithium Cobalt Oxide + 0.2 % Glucose



Sample: Lithium Cobalt Oxide + 1.0 % Glucose



Sample: Lithium Cobalt Oxide + 5.0 % Glucose

Fig. 3 Measurement Data

Visualization of the Additive Layer in Vicinity of Negative Electrode in Electrolyte Using SPM-8100FM and Electrochemical Solution Cell in Secondary Batteries

Introduction

The charging and discharging characteristics, durability, and other performance of secondary batteries, represented by lead acid batteries and lithium ion batteries, have been enhanced by addition of additives to the electrolyte. To date, however, how those additives contribute to improvement of battery performance still has not been clarified. Observation of the interface state in the vicinity of the negative electrode in the electrolyte is important for elucidating the contribution of the additive. This paper reports the first successful visualization of the lignin-lead (Pb) layer by cross-sectional imaging of the vicinity of the negative electrode (Pb) in a lead acid battery by using an SPM-8100FM high-resolution scanning probe microscope and an electrochemical solution cell. Use of the frequency modulation (FM) method in the SPM-8100FM enables detection of smaller force than is possible by conventional atomic force microscopy (AFM).

Akinori Kogure, Takenao Fujii

Lead Acid Batteries

Lead acid batteries are a type of secondary battery that possesses various advantages, including excellent safety, a wide operating temperature range, and discharge of a large current. For these reasons, they are widely used in uninterruptible power supply (UPS) devices, emergency power supply equipment for public facilities, and starting batteries for automotive engine start-stop systems, and thus have become an indispensable part of the social infrastructure. However, sulfation is known to be a problem in this type of battery, as it causes deterioration of battery performance^{(1), (2)}. Fig. 1 shows a schematic diagram of the sulfation phenomenon, in which lead sulfate generated by the discharge reaction is crystallized and hardened on the negative electrode. Additives are added to the dilute sulfuric acid used as the electrolyte in order to alleviate this problem. Sulfonated lignin⁽³⁾ (hereinafter, lignin) is a representative additive. However, even though observation by contact mode AFM has been reported, how lignin contributes to the electrochemical reaction and alleviation of sulfation still has not been clarified until now.

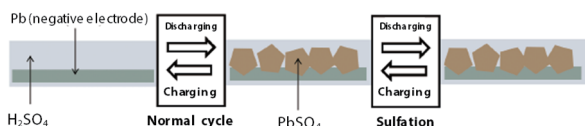


Fig. 1 Schematic Diagram of Negative Electrode and Sulfation

SPM-8100FM

Fig. 2 shows the SPM-8100FM. High-resolution observation and measurement is realized in this instrument by adoption of the frequency modulation method (FM method), which reduces noise in the atmosphere and in solutions to 1/20 of the conventional level.



Fig. 2 SPM-8100FM High-Resolution Scanning Probe Microscope

Results and Discussion

Fig. 3 and Fig. 4 show images of the vicinity of the negative electrode (Pb) by cross-sectional imaging after the initial reduction reaction (initial state as cell). In these, the sample is viewed from the cross-sectional direction. The upper part of the images is the dilute sulfuric acid side, that is, the electrolyte, and the position where the bright area in the lower part of the image changes to dark is the Pb surface. Parts where the probe detects force (repulsion) appear bright.

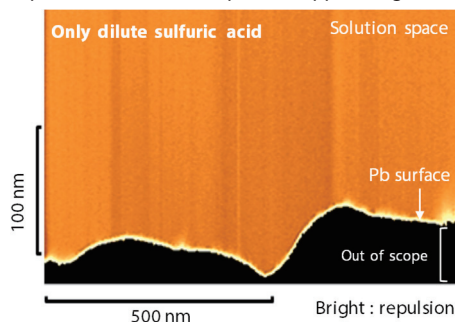


Fig. 3 Only Dilute Sulfuric Acid: Image of Vicinity of Negative Electrode (Pb) by Cross-Sectional Imaging

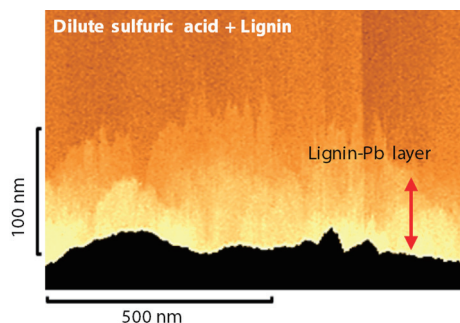


Fig. 4 Dilute Sulfuric Acid + Lignin: Image of Vicinity of Negative Electrode (Pb) by Cross-Sectional Imaging

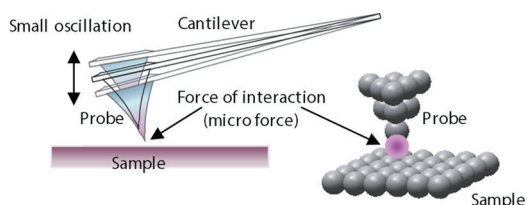
In the case of "Only dilute sulfuric acid" in Fig. 3, a distinctive contrast cannot be observed above the Pb surface. On the other hand, in the case of "Dilute sulfuric acid + lignin" in Fig. 4, a distinctive contrast can be seen above the Pb surface, as indicated by the red arrow in the figure. Because this distinctive contrast does not exist when only dilute sulfuric acid is used as the electrolyte, it is thought that this layer is a lignin-Pb, and this layer contributes to reduction of sulfation. The bright contrast of the lignin-Pb layer indicates that the probe has penetrated into the layer, and at the same time, also shows that the lignin-Pb layer is adsorbed on the Pb surface in a soft state. (Because lead is harder than the probe, the probe cannot penetrate into the Pb itself.)

Conclusion

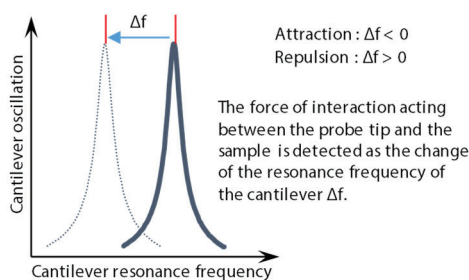
Cross-sectional imaging of the vicinity of Pb in dilute sulfuric acid was conducted using a SPM-8100FM and an electrochemical solution cell. As a result, it was possible to visualize a lignin-Pb layer having a thickness from 50 nm to 100 nm on the surface of the Pb after the initial reduction reaction for the first time. Application of analysis by cross-sectional imaging in electrolytes to analyses of other types of secondary batteries and the corrosion protection processes of metals can also be expected.

Principle

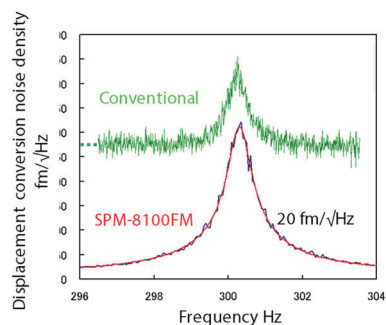
Fig.5 shows a schematic diagram of the frequency modulation method (FM method). Unlike the conventional amplitude modulation method (AM method), the FM method detects the force of interaction acting between the probe and the sample as a change of the resonance frequency of the cantilever Δf . By reducing the displacement conversion noise density to 20 fm/ $\sqrt{\text{Hz}}$ or less, cantilever oscillation can also be reduced in the SPM-8100FM method in comparison with the conventional technique. This enables detection of force in the atmosphere and in solutions with more than 20 times greater sensitivity than with the conventional AM method.



(a) Force of interaction acting between probe and sample



(b) Change of resonance frequency Δf due to micro force



(c) Resonance frequency and displacement conversion noise density

Fig. 5 Schematic Diagram of FM Method

Fig.6 shows the principle of cross-sectional imaging. The force received by the probe while changing the distance (Z direction) between the probe and the sample is measured as Δf by the force curve method. Cross-sectional imaging of the vicinity of the sample surface is possible by continuously scanning this in the X direction. The intensity of the force received by the probe is expressed by contrast in the image.

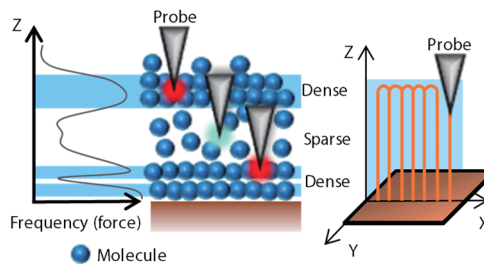


Fig. 6 Principle of Cross-Sectional Imaging

Experimental

Electrochemical solution cell

Fig.7 shows the electrochemical solution cell prepared for this experiment and the reaction formulas. The Pb plate working electrode, which corresponds to the negative electrode, is placed in a sulfuric acid aqueous solution (dilute sulfuric acid). The counter electrode is a Pb wire, and the reference electrode is a cadmium (Cd) wire. Oxidation (discharging) and reduction (charging) are possible by sweeping the voltage impressed on the Pb plate working electrode.

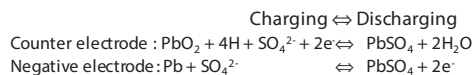
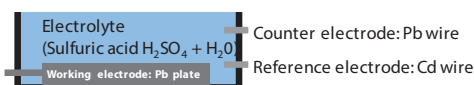


Fig. 7 Electrochemical Solution Cell and Reaction Formulas

Additive sulfonated lignin⁽³⁾

Fig.8 shows the structure of the sulfonated lignin (lignin) used as an additive. In dilute sulfuric acid, lignin exists as lignin-Pb. Improvement of battery performance as a result of the action of lignin-Pb as a surfactant and ion exchange resin is expected.

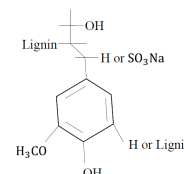


Fig. 8 Structure of Additive Lignin

Two electrolytes were prepared for this experiment, "Only dilute sulfuric acid" and "Sulfuric acid + lignin." Electrochemical solution cells, in which a Pb plate was set, were filled with the respective solutions, and an initial voltage sweep was conducted. Cross-sectional imaging of the interface between the Pb plate and the electrolyte was carried out after the reduction reaction in this sweep.

Reference

- (1) K. Hirakawa, S. Takahashi, M. Morimitu, Y. Yamaguchi, Y. Nakayama, YUASA-JIHO, NO. 87 (1999) pp. 42-26
- (2) S. Obuchi, M. Kyo, S. Inagaki, T. Takeuchi, H. Wada, Yuasa Technical Report, 2 (2016) pp. 15-21
- (3) Japan Storage Battery Co., Ltd., "Recent Practical Secondary Batteries - Selection and Use," (1995) pp. 213-2

This report is a revised version of the poster presented at the poster session of the 2018 Academic Lecture Meeting of The Japan Society of Vacuum and Surface Science by Takuhiro Watanabe^{*1}, Nobumitsu Hirai^{*2}, Akinori Kogure^{*3}, and Munehiro Kimura^{*1}.

*1 Nagaoka University of Technology

*2 National Institute of Technology, Suzuka College

*3 Shimadzu Techno-Research, Inc.

An Examination of the Effects of High/Low Column Cooling Rates Using Nexis™ GC-2030

Gas chromatography is a technique for separating components within a sample by utilizing the adsorption and desorption of components from a column when it is heated. The adsorption and desorption differ according to the column's liquid phase type. After analysis, the column must be cooled down to the initial temperature, but the rate at which the column is cooled may affect the column's liquid phase. Until now, priority was placed on shortening cooling times in order to shorten analysis cycles. However, the Nexis GC-2030 now allows operators to select a column cooling rate of their choice. By selecting the optimum cooling rate, the life time of the column can be maximized.

This article compares the baseline noise and the S/N ratio of peaks according to different cooling rates when using the Nexis GC-2030 cooling program.

A. Hashimoto

Column Liquid Phase

Fig. 1 shows the liquid phase model of a column coated with methyl phenyl polysiloxane. Each of the individual figures show the liquid phase structure in differing states: Fig. 1-1 at a high temperature, Fig. 1-2 at a low temperature, and Fig. 1-3 after rapid cooling.

At a high temperature, molecular mobility is increased and the liquid phase expands whereas at a low temperature the molecular mobility is suppressed and the liquid phase contracts. If the temperature change from high to low is gradual, the liquid phase expands and contracts without damaging its structure. However, if the column oven is cooled rapidly, the liquid phase is damaged as shown in Fig. 1-3 in which side chains with a large molecular structure in the liquid phase polymer are cut off.

The following sections study the affects of this damage on analysis results with respect to the stability and noise of the baseline and S/N ratios.

Baselines

Table 1 lists the gas chromatography (GC) analytical conditions used in this study and Fig. 2 shows the enlarged chromatogram of nine compounds. Using methanol as a solvent, a sample was prepared so that it contains the nine compounds indicated in Fig. 2 each at a concentration of 1 vol%. This sample solution was analyzed continuously 100 times using the analytical conditions listed in Table 1 with differing column cooling rates. Fig. 3 shows an enlarged view of the baseline of the 100th analysis with a low cooling rate (red line) and that with a high cooling rate (black line).

Looking at Fig. 3, we can see that the noise of the baseline is greater with the high cooling rate compared to that with the low cooling rate. This is because side chains in the column's liquid phase are cut off when using a high cooling rate and those chains are detected when the column is heated the next time around.

This result indicates that the cooling rate affects both the liquid phase of the column and the analysis results.

Table 1 GC Analytical Conditions

Model	: Nexis GC-2030/AOC-20i
Injection Mode	: Split mode
Injection Volume	: 1.0 µL
Split Ratio	: 1:50
Injection Temp.	: 250 °C
Carrier Gas	: He
Carrier Gas Control	: Constant linear velocity (30 cm/sec)
Column	: SH-Rtx™-50 (30 m × 0.32 mm I.D., 1.00 µm)
Column Temp.	: 40 °C (0 min.) - 4 °C/min. - 280 °C (0 min.)
Detector	: FID
Detector Temp.	: 320 °C
Detector Gas	: He 32.0 mL/min, Air 200 mL/min
Makeup Gas	: He (24 mL/min)

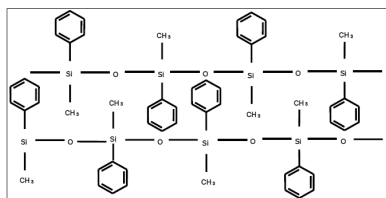


Fig. 1-1 Model of Liquid Phase Structure at High Temperature

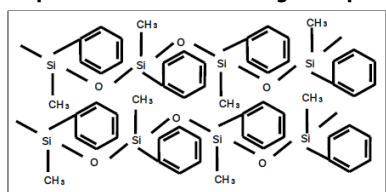


Fig. 1-2 Model of Liquid Phase Structure at Low Temperature

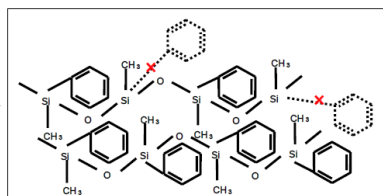


Fig. 1-3 Model of Liquid Phase Structure After Rapid Cooling

Fig. 1 Model Diagrams of the Column Liquid Phase

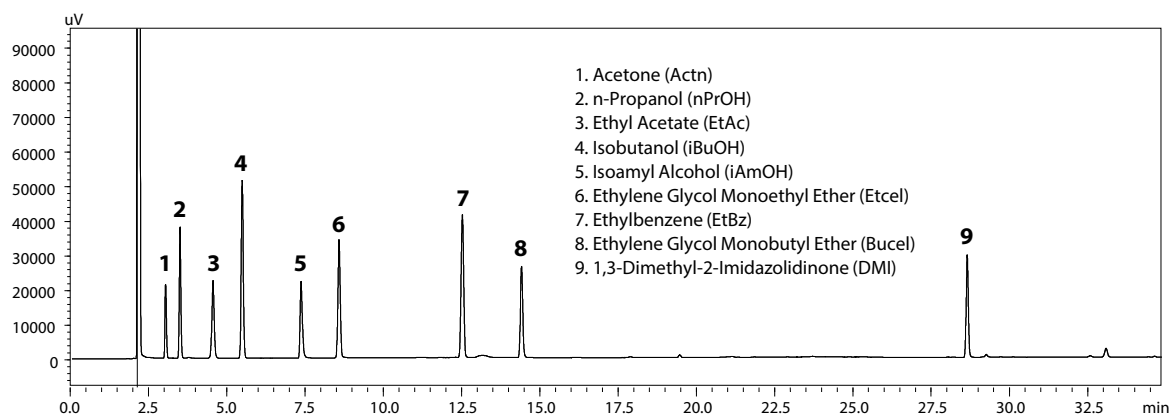


Fig. 2 Enlarged Chromatogram of Nine Compounds

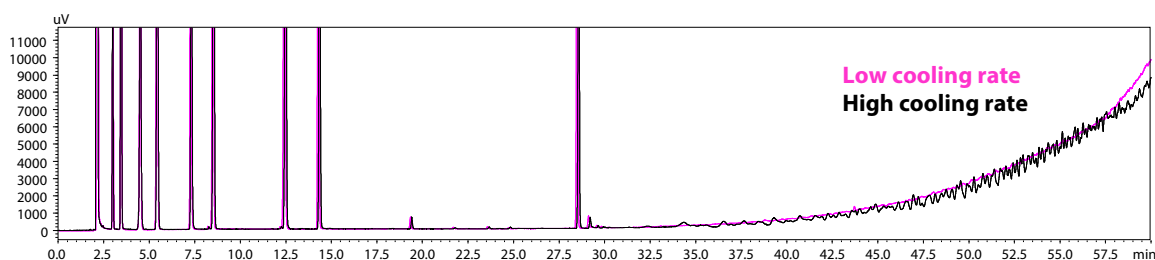


Fig. 3 Enlarged View of Baselines from the 100th Analysis with a High Cooling Rate and with a Low Cooling Rate

Table 2 Comparison of Noise and S/N Ratios

		Low Cooling Rate			High Cooling Rate		
		5th	50th	100th	5th	50th	100th
	Noise	128	81	76	631	284	259
1	Acetone	252	403	390	31	68	73
2	n-Propanol	310	494	525	60	129	151
3	Ethyl Acetate	170	264	297	34	65	81
4	Isobutanol	409	653	695	83	178	204
5	Isoamyl Alcohol	179	289	304	36	80	90
6	Ethylene Glycol Monoethyl Ether	270	430	460	55	120	136
7	Ethylbenzene	369	575	590	64	129	136
8	Ethylene Glycol Monobutyl Ether	211	346	362	43	97	107
9	1,3-Dimethyl-2-Imidazolidinone	249	358	378	50	105	115

■ Baseline Noise and S/N Ratios

Table 2 summarizes the baseline noise and the S/N ratios of the nine compounds from the 5th, 50th, and 100th analyses when using a fast cooling rate and when using a low cooling rate.

The values in Table 2 indicate that the baseline noise is smaller and S/N ratios are higher when using a low cooling rate compared to when using a high cooling rate.

When using a test method involving S/N ratios, using a low cooling rate is likely to be effective.

■ Conclusion

When performing analyses repeatedly on a gas chromatograph, the cooling conditions for the oven may affect the liquid phase of the column depending on its type.

Until now, gas chromatographs were designed with an openable flap on the back side so that cooling times can be shortened and thereby shorten analysis times.

The Nexis GC-2030 allows operators to select the optimum cooling rate for the column that is used. This can maximize the column performance over a long use period while also enabling the acquisition of favorable analysis results.

Rtx is a registered trademark of Restek Corporation.

First Edition: May 2018

High-Sensitivity Simultaneous Analysis of Inorganic Gases and Light Hydrocarbons using Nexis GC-2030 Dual BID System

Analyses for inorganic gases and light hydrocarbons are implemented in a variety of fields including petrochemistry, catalysts, batteries and other resource and energy fields, and environmental fields.

The barrier discharge ionization detector (BID) installed in Nexis GC-2030 gas chromatograph is capable of detecting a wide variety of components with high sensitivity*. Thanks to Shimadzu's proprietary barrier discharge technology, this detector features high sensitivity while maintaining the same level of stability as the previous general-purpose detectors.

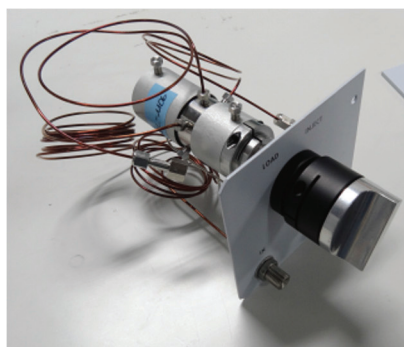
In this Application News, we introduce a high-sensitivity simultaneous analysis of inorganic gases and light hydrocarbons using Nexis GC-2030 gas chromatograph, which is equipped with two columns and two BID detectors.

*Unable detect to helium and neon

T. Yokoya, T. Murata

■ Instruments and Analytical Conditions

In this analysis, the MGS-2030 gas sampler was used for the introduction of gas into the instrument; the column was connected using the SPLITTER-INJ. The MGS-2030 is a manual gas sampler. A purge mechanism is included to reduce the leakage of peripheral air into the system. The SPLITTER-INJ refers to a special injection unit that permits split injection of the sample without requiring that it pass through the standard split/splitless injection unit. Using the MGS-2030 for sample gas injection together with the SPLITTER-INJ unit, it is possible to quantitatively analyze trace level air components, including Oxygen (O₂), Nitrogen (N₂), etc., with high accuracy.



Valve Unit



Manual Flow Controller for Purge

Fig. 1 MGS-2030 Gas Sampler

Table 1 Analytical Conditions

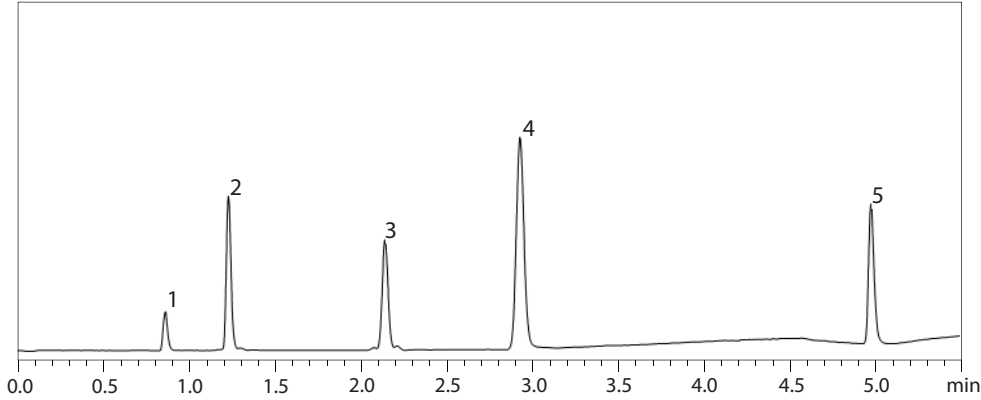
Model	: Nexis GC-2030
Detector	: BID-2030
Gas Sampler	: MGS-2030
Column	: Line1: Rt-Msieve 5A (0.32 mm I.D. × 15 m, d.f. = 30 μm) Line2: Rt-Q-BOND (0.32 mm I.D. × 30 m, d.f. = 10 μm)
Column Temperature	: 40 °C (3 min) - 40 °C /min - 200 °C (2 min) Total 9 min
Injection Mode	: Split 1 : 10
Purge Gas	: 3 mL/min (He)
Carrier Gas Controller	: Pressure (He)
Pressure Program	: 114 kPa (5 min) - 100 kPa/min - 200 kPa (3.14 min) Total 9 min
Detector Temperature	: 280 °C
Discharge Gas	: 50 mL/min (He)
Injection Volume	: 1 mL

■ Analysis Results

Only specific types of separation columns can be used for separation of inorganic gases and light hydrocarbons, and it is sometimes impossible to use a single column to separate all of the target components. Utilizing a dual

capillary column system, constructed using two detectors and two columns, enables faster, higher separation analysis of inorganic gases and light hydrocarbons than methods using only one column.

Line 1 Rt-Msieve5A Column



- 1: Hydrogen
- 2: Oxygen
- 3: Nitrogen
- 4: Methane
- 5: Carbon monoxide
- 6: Air + Carbon monoxide
- 7: Methane
- 8: Carbon dioxide
- 9: Ethylene
- 10: Acetylene
- 11: Ethane
- 12: Water

Line 2 Rt-Q-BOND Column

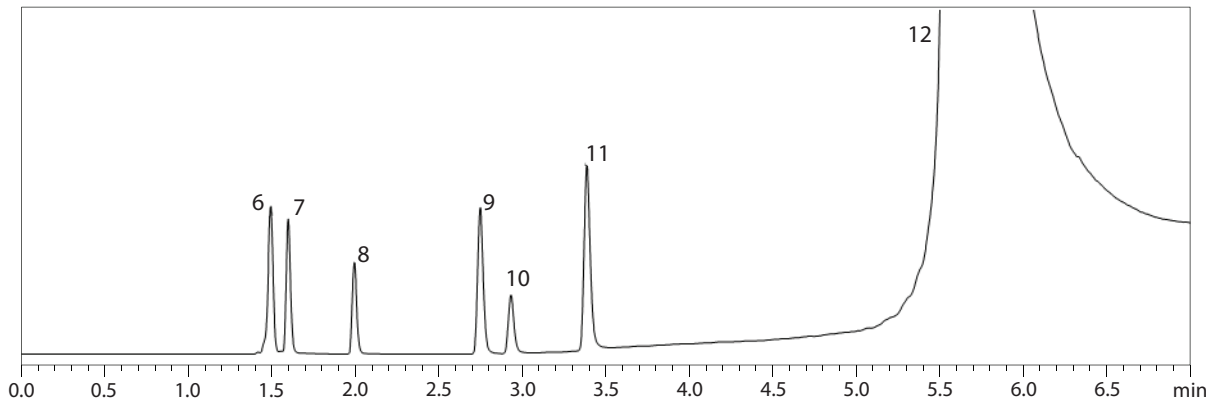


Fig. 2 Chromatogram for 5 ppm Mixed Gas* * Helium balance

Table 2 Repeatability of Area Values ($\mu\text{V} \times \text{sec}$) for Each Component

	1	2	3	4	5	6	Ave.	RSD%
Hydrogen	3996	4010	4040	4052	4096	4105	4050	1.10
Oxygen	15036	14983	15023	14973	15009	15067	15015	0.23
Nitrogen	17021	16490	16510	16472	16566	16589	16608	1.25
Methane	35142	35412	35561	35625	35784	35970	35582	0.81
Carbon monoxide	17143	17237	17330	17371	17441	17499	17337	0.76
Carbon dioxide	25817	25812	25829	25779	25925	26010	25862	0.34
Ethylene	49433	49439	49527	49481	49714	49833	49571	0.33
Acetylene	37416	37436	37446	37440	37604	37717	37510	0.33
Ethane	67092	67187	67263	67357	67579	67701	67363	0.35

Trace Impurity Analysis of Hydrogen Fuel in Fuel Cell Vehicle-Related Fields

With the development of fuel cell technology for electricity generation using hydrogen (H) as fuel, attention is turning to household fuel cell systems and fuel cell vehicles. However, one of the problems associated with fuel cells in their current state is the presence of carbon monoxide (CO) in the hydrogen fuel used in the fuel cells. Carbon monoxide adversely affects the performance of the catalyst used in the battery. This phenomenon is referred to as "catalyst poisoning," and therefore necessitates the use of high-purity hydrogen fuel. The international standard (ISO 14687-2) pertaining to hydrogen fuel for fuel cell vehicles, which went into effect in 2012, specifies that, in addition to a maximum concentration of 0.2 ppm carbon monoxide in the hydrogen, maximum concentrations are also specified for oxygen (O) and carbon dioxide (CO₂) as well as hydrocarbons. In the past, analysis of impurities in hydrogen conventionally required a complex system including multiple detectors and columns, which from the standpoint of cost and maintenance, posed a significant hurdle.

The barrier discharge ionization detector (BID) is a new, universal detector that can detect almost all components, except helium (He, used as the plasma gas) and neon (Ne), with higher sensitivity than that obtained using TCD and FID detectors. This Application News introduces an example of high-sensitivity analysis of carbon monoxide in hydrogen and simultaneous analysis of impurities in hydrogen using the Tracera high-sensitivity gas chromatograph equipped with a BID detector.

High-Sensitivity Analysis of Carbon Monoxide Using the Rt-Msieve 5A Column

Molecular sieve 5A columns offer good separation of air components and carbon monoxide, and are a suitable type of column for the analysis of carbon monoxide.

First, a standard gas was diluted with hydrogen to adjust the concentration of each component (excluding air components) to about 0.2 ppm, and measurement of the gas was then conducted using the Rt-Msieve 5A column.

The chromatogram is shown in Fig. 1, and the analytical conditions are shown in Table 1. The lower limit of detection (S/N=3) of carbon monoxide was then calculated as 0.032 ppm.

Table 1 Analytical Conditions for Trace Impurities in Hydrogen (Rt-Msieve 5A column)

Model	: Tracera (GC-2010 Plus + BID-2010 Plus)
Column	: RESTEK Rt-Msieve 5A (30 m × 0.53 mm I.D., df = 50 μm) with Particle Trap 2.5 m
Column Temp.	: 35 °C (2.5 min) → 20 °C/min → 250 °C → 15 °C/min → 270 °C (3.42 min)
Inj. Mode	: Split 1:7
Carrier Gas Controller	: Constant linear velocity mode (He)
Linear Velocity	: 45 cm/sec
Det. Temp.	: 280 °C
Discharge Gas	: 50 mL/min (He)
Inj. Volume	: 3 mL

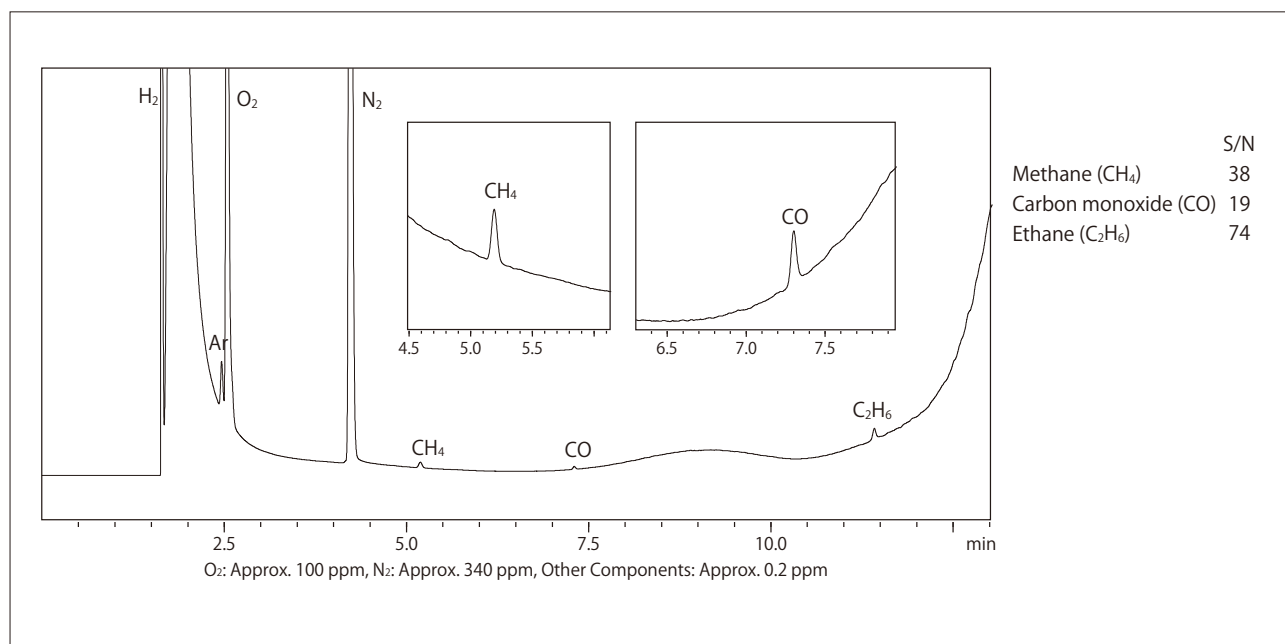


Fig. 1 Chromatogram of Trace Impurities in Hydrogen (Rt-Msieve 5A Column)

■ Simultaneous Analysis of Impurities in Hydrogen Using the Micropacked ST Column

As carbon dioxide does not elute with the Rt-Msieve 5A column, a different system is required for analysis when carbon dioxide is among the target substances. The Micropacked ST column supports separation of inorganic gasses, including carbon dioxide and lower hydrocarbons, making it suitable for simultaneous analysis of impurities in hydrogen gas.

A standard gas was diluted with hydrogen to adjust the

component concentrations (other than air components) to about 0.2 ppm, and this gas was analyzed using the Micropacked ST column.

The resultant chromatogram is shown in Fig. 2, and the analytical conditions are shown in Table 2. The lower limit of detection of carbon monoxide was calculated as 0.078 ppm ($S/N=3$). Though not as good as those obtained with the Rt-Msieve 5A column, the results include detection of the maximum concentration stipulated by ISO 14687-2.

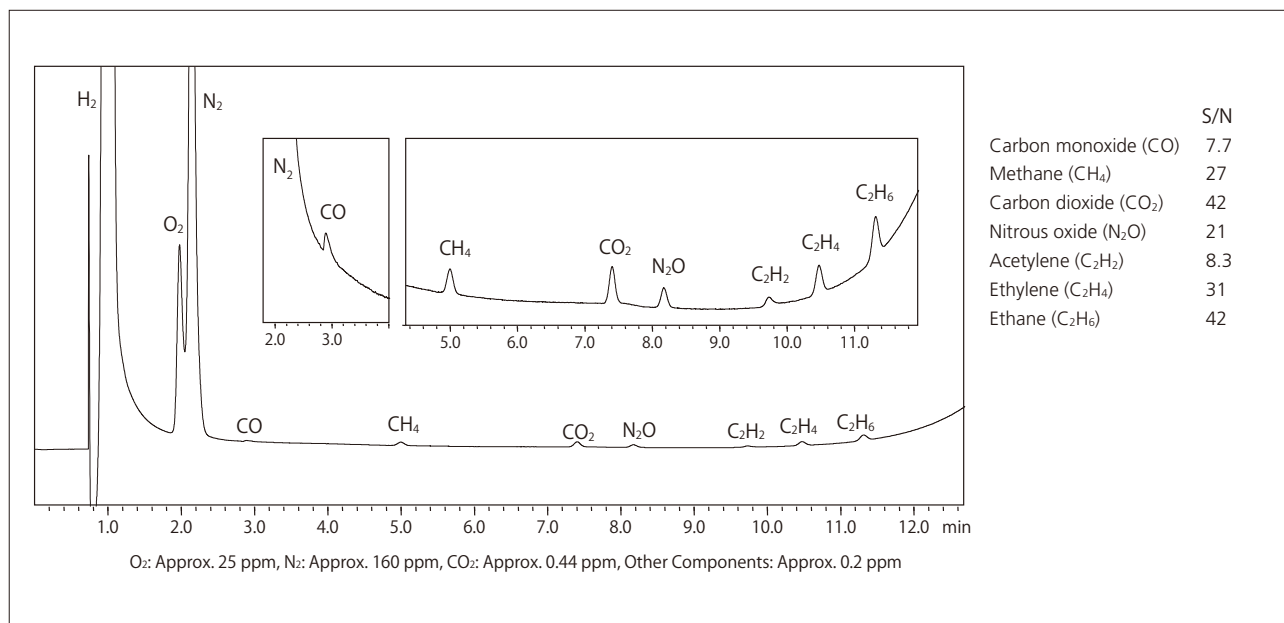


Fig. 2 Chromatogram of Simultaneous Analysis of Impurities in Hydrogen (Micropacked ST Column)

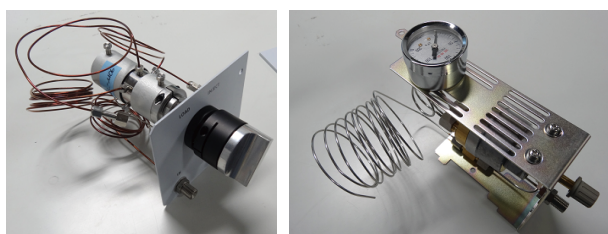
Table 2 Analytical Conditions for Simultaneous Analysis of Impurities in Hydrogen (Micropacked ST Column)

Model	: Tracera (GC-2010 Plus + BID-2010 Plus)
Column	: Micropacked ST (2 m × 1 mm I.D.)
Column Temp.	: 35 °C (2.5 min) → 20 °C/min → 250 °C → 15 °C/min → 265 °C (3 min)
Inj. Mode	: Split 1:4
Carrier Gas Controller	: Pressure mode (He)
Pressure Program	: 226.8 kPa (2.5 min) - 15 kPa/min - 400 kPa (3.2 min)
Det. Temp.	: 280 °C
Discharge Gas	: 50 mL/min (He)
Inj. Volume	: 3 mL

In this analysis, the MGS-2010 gas sampler was used for the introduction of gas into the instrument; the column was connected using the SPLITTER-INJ (P/N: 221-76252-41).

The MGS-2010 is a manual gas sampler for the Tracera (GC-2010 Plus). A purge mechanism is included to reduce the leakage of peripheral air into the system. The SPLITTER-INJ refers to a special injection unit that permits split injection of the sample without requiring that it pass through the standard split/splitless injection unit.

Using the MGS-2010 for sample gas injection together with the SPLITTER-INJ unit, it is possible to quantitatively analyze trace level air components, including Oxygen (O₂), Nitrogen (N₂), etc., with high accuracy.



Valve Unit

Manual Flow Controller for Purge

Fig. 3 MGS-2010 Gas Sampler

Confirmation of Synthesis of Organic Functional Materials Using Benchtop MALDI-TOF MS

The Matrix-Assisted Laser Desorption/Ionization Time-of-Flight Mass Spectrometer (MALDI-TOF MS) has the advantage of simply and quickly obtaining molecular weight information on diverse types of samples from low molecular to macromolecular materials. MALDI-TOF MS instruments are widely used in confirmation of the molecular weights of synthetics and natural substances in the field of R&D and quality control.

In comparison with LC-MS and other types of mass spectrometers, MALDI-TOF MS enables use of diverse solvents, is quick and simple in optimizing acquisition parameters, and detects mainly the peaks of singly charged ions (one component = one peak), even with samples having large molecular weights. Due to these advantages, it is possible to confirm synthesis of organic functional materials such as organic dyes, organic light-emitting diode (OLED) materials, and organic photovoltaic cells simply and quickly.

Here, we introduce examples of measurement of various types of organic functional materials using a benchtop MALDI-TOF MS.

K. Shima

Sample Pretreatment

The sample materials used here were commercially-available organic functional materials purchased from Tokyo Chemical Industry Co., Ltd. or Sigma-Aldrich Co. LLC. These samples were dissolved in THF (tetrahydrofuran) so as to obtain a concentration of approximately 1 mg/mL. The sample solutions were spotted on a stainless steel plate for MALDI measurement together with a matrix (DCTB (trans-2-[3-(4-tert-butylphenyl)-2-methyl-2-propenylidene] malononitrile), 10 mg/mL THF solution) and dried. Measurements were then carried out using a Shimadzu MALDI-8020 benchtop MALDI-TOF MS (Fig. 1).

Examples of Measurement of Organic Functional Materials

As examples of measurements of organic functional materials, Fig. 2 shows the mass spectra of polymeric semiconductor building blocks and an OLED material. The singly charged radical cations of the respective samples were measured with good S/N ratios, and the patterns of the measured isotopic distributions also showed good agreement with the theoretical isotopic distributions. These results demonstrate that confirmation of synthetic products is possible not only from the measured mass of the molecular ion but also from the isotopic distribution pattern when using MALDI-TOF MS.



Fig. 1 MALDI-8020 Benchtop MALDI-TOF MS

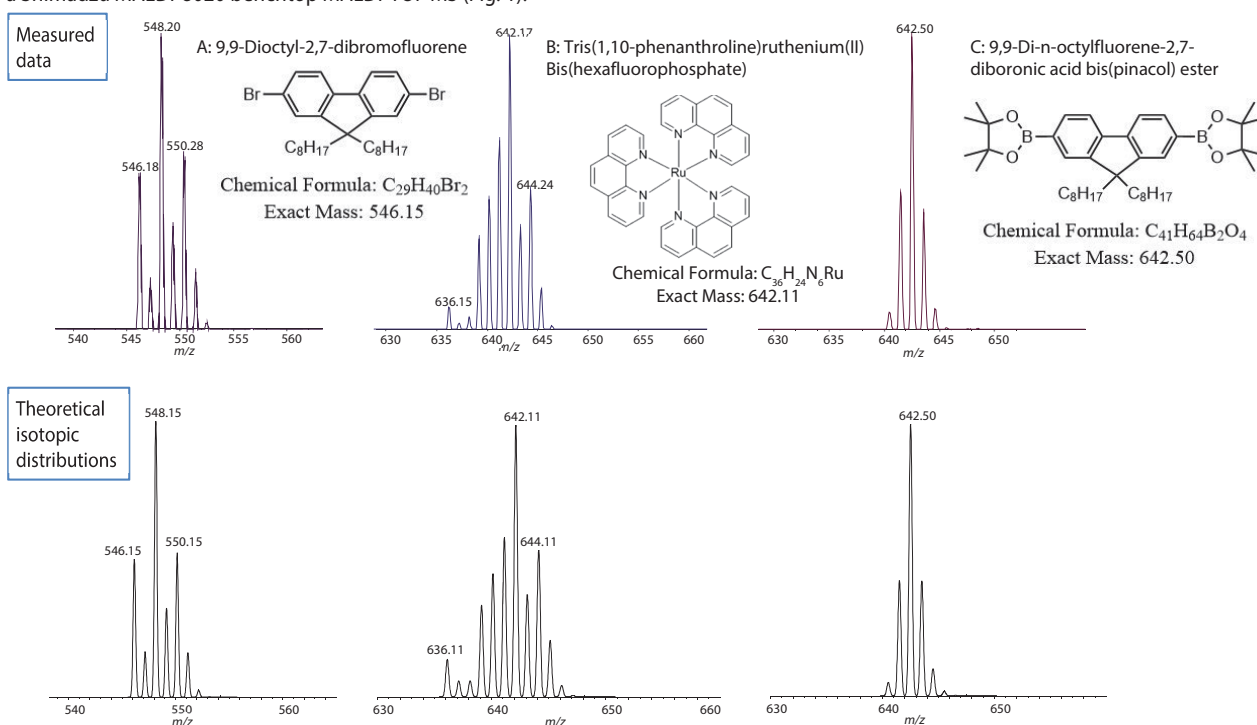


Fig. 2 Mass Spectra of Polymeric Semiconductor Building Blocks (A, C) and OLED Material (B)
Top: Measured data, Bottom: Theoretical isotopic distributions

*Structural Formulae from Website of Tokyo Chemical Industry Co., Ltd.

Examples of Measurement of Organic Functional Materials with Molecular Weights Exceeding 1,000 Da

It is possible to obtain similar data for organic compounds having molecular weights of less than 1,000 Da, as shown in Fig. 2, by using DART® (Direct Analysis in Real Time), which is a direct ionization method. However, the difficulty of ionizing molecules having molecular weights exceeding 1,000 Da is a problem with DART-MS. Since organic functional materials include substances with molecular weights exceeding 1,000 Da, the range that can be covered by DART is limited.

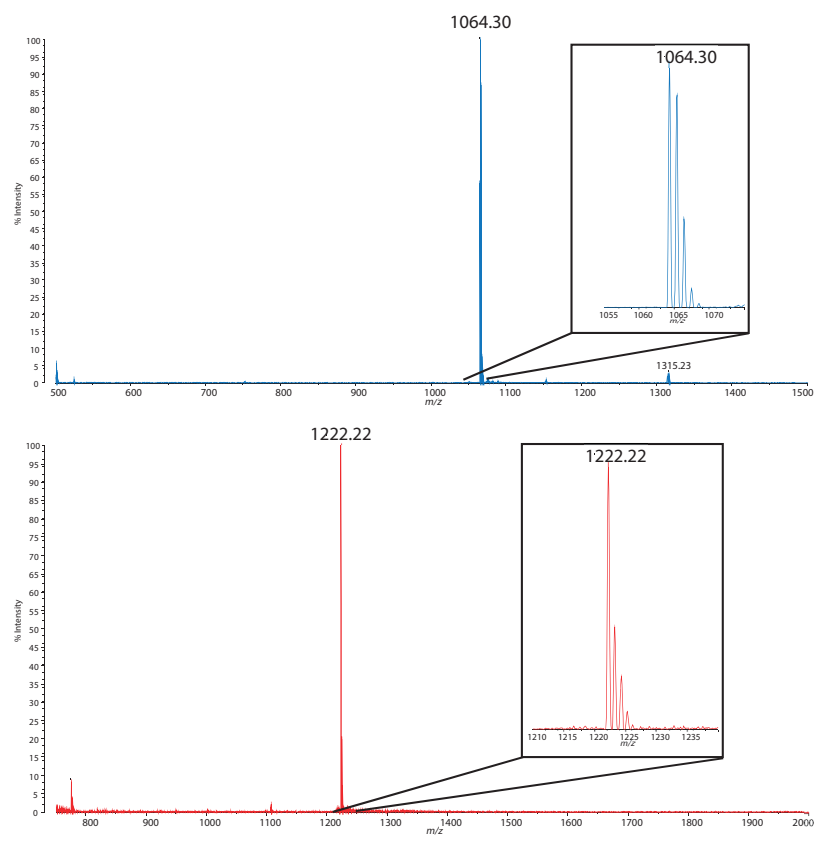
Because MALDI-TOF MS enables measurement of a greatly wider mass range than is possible with DART, molecules with molecular weights greater than 1,000 Da can also be ionized easily. Therefore, molecules having molecular weights exceeding 1,000 Da among fullerenes and metallic complexes used as materials for organic photovoltaic cells were measured by MALDI-TOF MS as test materials (Fig. 3). For both of these examples, singly charged radical cations were measured with good S/N ratios and, from the enlarged figure, it can be observed that good separation of the respective isotopic peaks was also obtained.

Conclusion

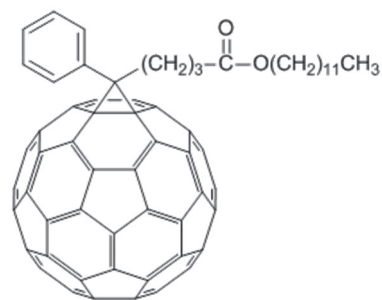
This experiment showed that the MALDI-8020 benchtop MALDI-TOF MS is capable of measuring organic functional materials such as OLED and organic photovoltaic cells with molecular weights exceeding 1,000 Da. Not limited to these materials, MALDI-TOF MS is also effective for confirmation of synthesis of various types of organic functional materials and their synthetic intermediates because it is possible to measure substances that are difficult to measure with other types of mass spectrometers (e.g. organic compounds with low solubility or comparatively large molecular weights and complex structures).

Recent MALDI-TOF MS instruments have become increasingly complex and large in scale simultaneously with the development of higher performance specifications. As a result, those systems may be over-specification for measurement needs using the linear mode, which account for a large part of MALDI applications, and their size and purchase/maintenance costs are also substantial hurdles to system introduction.

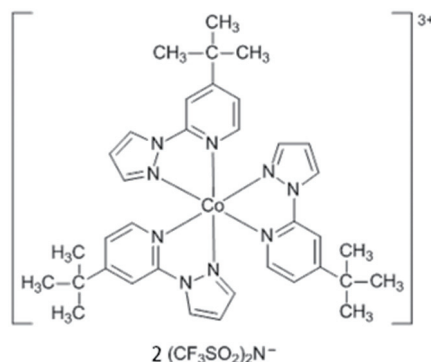
In contrast, the MALDI-8020, which offers ample performance for confirmation of synthetic products in spite of its compact size, is a product that satisfies the measurement needs of organic functional materials. Future development is expected.



[6,6]-Phenyl-C₆₁-butyric Acid Dodecyl Ester



Tris[4-tert-butyl-2-(1H-pyrazol-1-yl)pyridine]cobalt(III) Bis(trifluoromethanesulfonyl)imide



Investigating the surface and interface of Li ion thin-film battery materials

No. MO435

Overview

There is a growing need to develop smaller more efficient energy storage materials to support the widespread use of portable electronic devices such as smart phones and tablets. The use of Lithium ion batteries was first proposed in 1973 with Li^+ ions acting as charge carriers moving to the positive electrode during use and then changing direction during charging. The technology was commercialised in 1991 and has since superseded nickel hydride as the battery material for consumer electronics applications. More recently Li ion batteries are replacing lead-acid batteries for bulkier vehicle and aerospace applications.

Classical lithium ion batteries rely on a liquid electrolyte however there have been significant developments towards replacing liquid electrolytes with solid state thin-films. Thin-film lithium ion batteries offer improved performance by having a higher average output voltage, lighter weights thus higher energy density, and longer cycling life than typical liquid electrolyte batteries. In order to construct a thin film battery it is necessary to fabricate all the battery components, as an anode, a solid electrolyte, a cathode and current leads into multi-layered thin film. Lithium phosphorous oxynitride (LiPON) is widely used in solid state micro-batteries due to low electronic conductivity, increased durability to cycling and ease of preparation. Despite the widespread use of LiPON much is still unknown regarding Nitrogen bonding and Li mobility.

Here we will use conventional surface analysis techniques of XPS and sputter depth profiling to understand the surface and bulk chemistry of LiPON films formed via atomic-layer deposition (ALD). XPS yields quantitative information regarding the elemental composition of the near surface region to a depth of <10 nm. The elemental composition as a function of depth is probed and comparisons are made between the results obtained from conventional monatomic depth profiling and cluster depth profiling.

Experimental

All measurements were performed using the AXIS photoelectron spectrometer equipped with the gas-cluster ion source (GCIS). For these experiments the GCIS was run in high-energy cluster mode using 20 kV Ar_{1000}^+ . High-energy cluster ions were used to enable depth profiling to be performed in a practical time frame. Sample rotation was used throughout the profiles to reduce the effects of sputter roughening and layer blending. LiPON thin-films were produced by ALD using Li precursors and a N_2 plasma [1]. LiPON films were previously characterized by optical ellipsometry to be ~50nm thick.

Results and Discussion

After introduction into the analysis chamber a survey spectrum was acquired from the as-received sample. Analysis of the survey spectrum showed presence of the constituent elements Li, P, O and N and also a significant amount of carbon which can be attributed to the presence of adsorbed species from air exposure. To examine the distribution of Li throughout the film, depth profiling was performed. Figure 1 shows comparison of conventional monatomic depth profiling using 4 kV Ar^+ ions and the same sample profiled with 20 kV Ar_{1000}^+ ions. Both depth profiles were performed as an overnight experiment with the cluster mode etch rate >4nm/min.

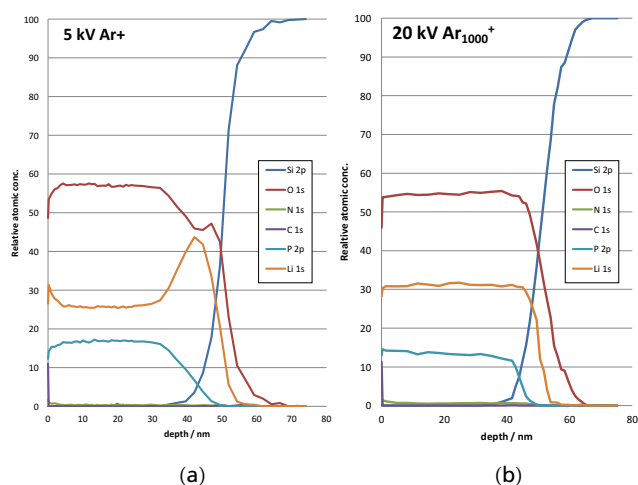


Figure 1:
Depth profile of 50 nm LiPON thin-film using
(a) 5 kV Ar^+ (b) 20 kV Ar_{1000}^+

There is a distinct difference between the two profiles. Under monatomic bombardment there is an initial increase in Li concentration after the first etch cycle – a consequence of removing surface contamination – then a subsequent decrease in Li into the bulk of the film reaching a steady-state of ~25.5 atomic%. Near the LiPON interface with Si substrate the Li concentration increases significantly reaching a maximum of 44%. By contrast when profiled 20 kV Ar_{1000}^+ ions the profile shows a different distribution of Li. An initial increase in Li concentration is shown after the first etch however there is no subsequent decrease reaching a steady-state of >31%. This amounts to an increase of 22% Li throughout the film depth compared to the monatomic profile. Interestingly no accumulation of Li was seen at the interface with the Si substrate. A comparison of the Li concentrations profiled using two different ions is shown in figure 2.

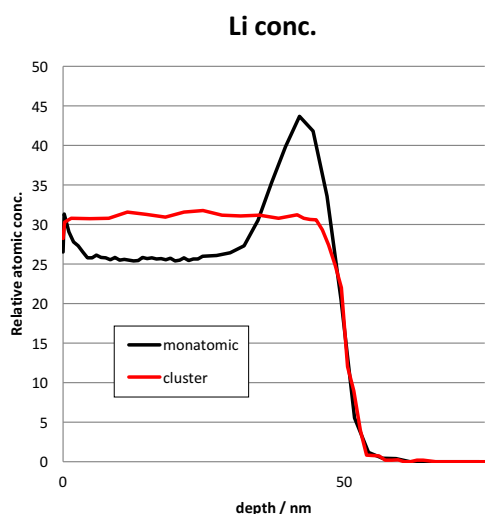


Figure 2:
Li ion concentration comparison between monatomic (black) and cluster profile (red)

Previously monatomic Ar^+ bombardment of glasses has shown lower than expected concentrations of light elements such as sodium [2]. This phenomenon was attributed to positive charge build-up in the near surface region from implanted Ar^+ ions. The charge build-up repels the small, mobile positive ions in the surface further into the bulk resulting in an underestimation in surface quantification. The same mechanism of Li ion repulsion and bulk migration is proposed to occur for LiPON thin-films analysed here. Li migration occurs under monatomic profiling resulting in an underestimation of Li concentration. Repulsive bulk migration also accounts for the increase in Li concentration at the interface with the Si substrate. The light ions are unable to penetrate through into the native Silicon oxide and instead accumulate at the interface. It must be noted that this system is particularly susceptible to this process because the Li^+ ions in LiPON by their design are mobile for the charge transfer process.

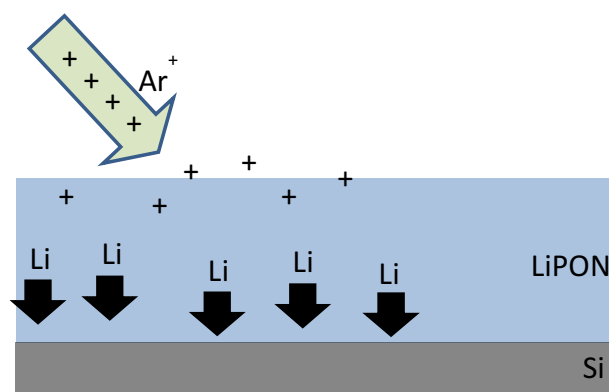


Figure 3: Schematic of ion action on light elements.

Conclusion

It has been demonstrated that the use of XPS combined with depth profiling techniques provide quantitative information on the composition of LiPON thin-films created via ALD. It has been shown that the use of monatomic Ar^+ ions is unsuitable for profiling materials with mobile, light elements as the build-up of positive charge can cause migration leading to incorrect stoichiometry. It is concluded that the use of high energy Ar_n^+ clusters for depth profiling this class of materials is vital to mitigate the effects of ion migration and gain confidence in the validity of the results.

Acknowledgements

Many thanks to the research group of Prof. Gary Rubloff and in particular Alex Pearse at the University of Maryland.

References

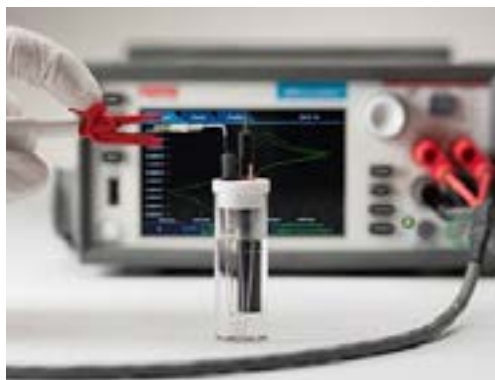
1. A. Kozen, A. Pearse, G. Rubloff, C-F Lin, M. Noked, Chem. Mater., 2015, 27, 5324–5331
2. Y. Yamamoto, K. Yamamoto, J. Non. Cry. Sol., 2015, 356, 14

Distribution, segregation and chemical state identification of Lithium salts on Cu electrodes

Introduction

Rechargeable metal-based batteries (Li, Na and Al) are among the most versatile platforms for high-energy storage. Unfortunately however there are several pitfalls for these energy storage systems, one of which is deposition and dendrite formation during repeated cycles of charge and discharge. Many studies have been performed in search of a dendrite-free, deposition-free system for lithium batteries using novel materials such as 3D structures and carbon nanofibers.^[1,2]

Here we will explore the distribution of Lithium in different chemical environments on electrode surfaces. We employ conventional surface analysis techniques (XPS) to yield large area, quantitative, information regarding the distribution of surface species. To explore the lateral and depth distribution of Li we also utilise XP imaging and Argon cluster depth profiling.



Experimental

XPS was performed using the state-of-the-art AXIS spectrometer. Survey spectra were acquired over a large energy range of 0 to 1200 eV. The co-axial charge neutraliser was used to mitigate against charge build-up. Depth profiling was performed using Argon cluster ions (20kV Ar₅₀₀⁺).^[3] High spatial resolution XPS images were acquired over a large surface area using stitched imaging mode.

This imaging mode combines fast parallel imaging with stage movements. In this example a 3x3 stitched image using a 400µm field of view provided an image of 1.2 x 1.2 mm. Small-spot spectroscopy was performed using a 110 micron diameter aperture and the total acquisition time for each survey spectrum was 4 minutes. After synthesis of the electrodes, CV experimentation was performed via the three electrode system.^[4]

Results

XPS survey spectra were acquired for different areas of the electrode surface (figure 1). Peak identification showed the presence of expected elements - Mg, Li, Cu, O and C on the surface post experiment, also present were low levels of other elements, most probably contamination – F, Na, Cl, S (see table 1).

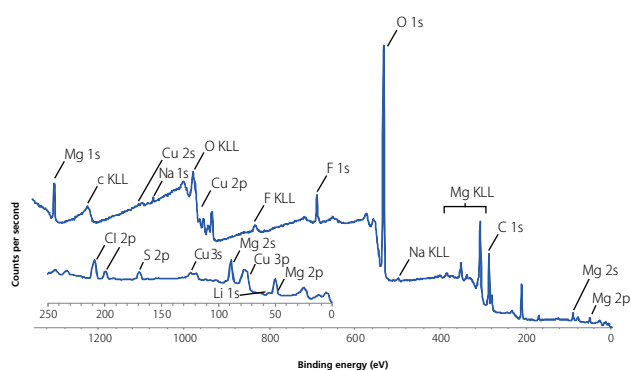


Figure 1: Large area survey spectrum of electrode surface.

Table 1: Surface quantification of as-received electrode surface.

Element	Quantification
	Atomic conc. [%]
Mg	3.91
Cu	3.79
O	55.00
F	5.15
C	20.81
S	0.99
Cl	0.53
Na	0.24
Li	9.57

The distribution of Li into the bulk of the electrode surface was further explored using Argon cluster depth profiling. A high-energy cluster (20kV Ar₅₀₀⁺) ion was used to allow for quick, deep, depth profiling whilst limiting the migration of light Li ions – a common issue with monatomic Argon depth profiling. Figure 2 shows the distribution of surface species as a function of etch time.

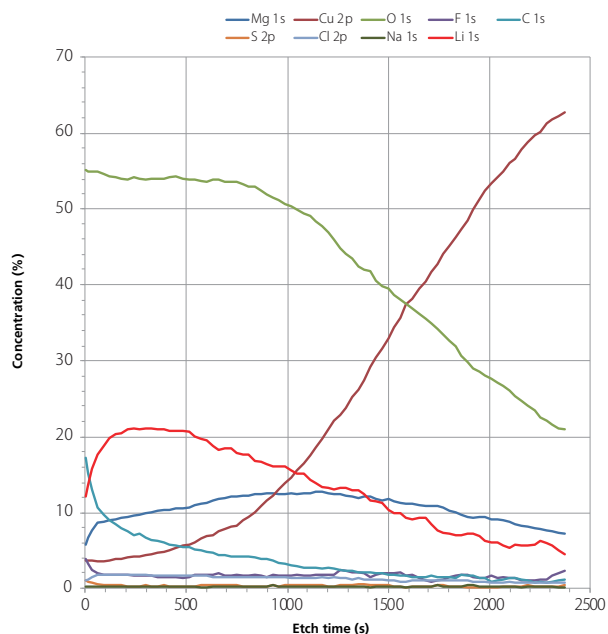


Figure 2: 20 kV Ar₅₀₀⁺ depth profile of electrode surface.

After the first few etch cycles the concentration of Li increases to >20 at.%. Further sputter removal of surface material shows a decrease in Li concentration. This indicates that Li is segregated into the uppermost region of the electrode surface and the Li concentration decreases once the depth profile had reached the interface with the Cu bulk electrode surface. There is little evidence to suggest that Li has migrated deeper into the electrode.

Using the in-situ optical microscope on the analysis chamber it was possible to identify white crystallite structures on the electrode surface (figure 3a). By acquiring peak-minus-background stitched images at fixed energies for different elements it is possible to observe the relative distributions and accumulations of particular species on the surface. XPS images were acquired for several of the elements identified in the survey spectrum to investigate the composition of these crystallites (figure 3b-c). Here we can see that there is a higher concentration of Cl on the crystallite regions when compared to the rest of the electrode surface. Conversely there is a decrease in the atomic concentration of Mg. A combined overlay image of the two elemental XPS images highlights the distinctive distribution differences of the elements (figure 3d).

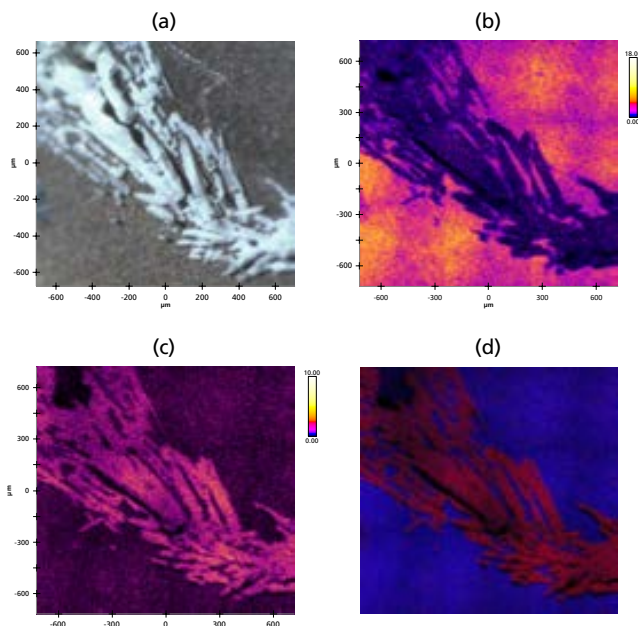


Figure 3:
(a) Optical microscope image of surface crystallites;
(b) XPS stitched image of Mg;
(c) XPS stitched image of Cl;
(d) overlay of Mg (blue) and Cl (red).

Using the XPS images for navigation it was possible to acquire small-spot, selected area spectroscopy both on and off the crystalline regions (figure 4). Elemental quantification from the electrode and crystalline survey spectra are shown in Table 2.

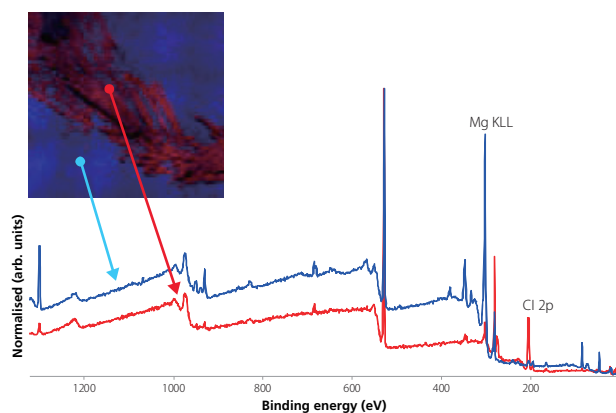


Figure 4: 110 micron small-spot survey spectra on electrode (blue) and crystallite (red) areas.

Table 2: Surface quantification of electrode and crystallite areas.

Element	Quantification	
	BLUE (electrode)	RED (crystalline)
Mg 1s	5.24	0.97
Cu 2p	2.46	0.36
O 1s	50.49	42.30
F 1s	3.79	1.52
C 1s	31.59	34.56
S 2p	1.18	0.46
Cl 2p	2.66	10.75
Li 1s	2.00	8.97
Na 1s	0.59	0.11

As indicated from the images we see a high accumulation of Cl on the crystalline areas along with a significantly higher concentration of Li. The atomic concentration of F, S, Na were depleted in the crystalline regions. To further elucidate the nature of these crystalline areas high energy resolution, chemical state, spectra were acquired (figure 5). As expected there is a significantly higher Cl signal for the crystalline areas. Peak-fitting analysis of both spectra indicates three different chemical environments for Cl: perchlorate ion (208.6 eV), chlorate (206.6 eV) and chloride (198.8 eV). For the crystalline areas the most dominant chemical state of chlorine is in the perchlorate ion. This along with the increased concentration of Li in this region (and decreased concentrations of other non-electrode surface species) indicates that the white crystalline species is Lithium perchlorate.

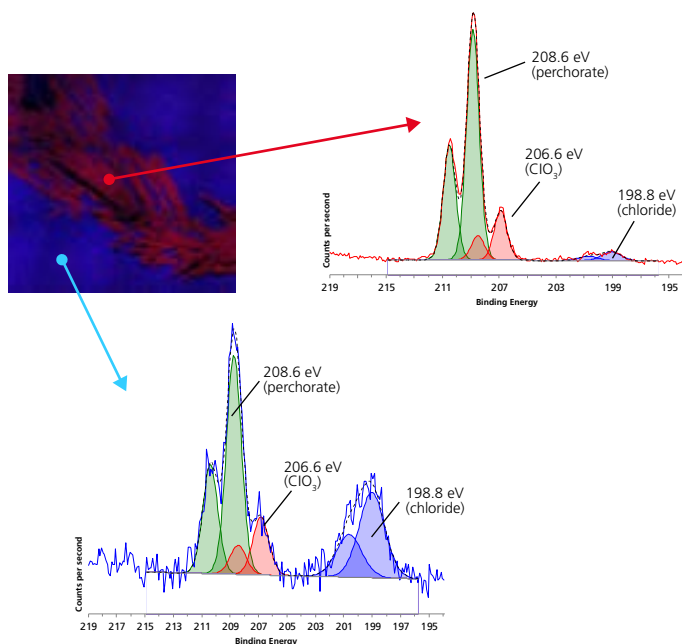


Figure 5: 110 micron small-spot spectroscopy of Chlorine 2p region for electrode (blue) and crystallite (red) areas.

Conclusion

XPS was used to investigate the distribution of Li and other surface species on Cu electrode surfaces. Applying argon cluster depth profiling it was possible to observe that the Li is contained within the surface of the electrode and has not penetrated into the bulk. Crystalline species were identified on the surface of the electrode as Lithium perchlorate.

Acknowledgements

Many thanks to Dr. Narayanan at TFIR who provided both samples and fruitful discussion.

References

1. J. Xiang, Y. Huang et al., *Nano Energy*, 42, 2017, 262-268.
2. Y. Yuan, C. Wu et al., *Energy Storage Materials*, 16, 2019, 411-418.
3. www.kratos.com/products/arn-ion-source [accessed 3/1/19].
4. Bard, Allen J.; Larry R. Faulkner (2000-12-18). *Electrochemical Methods: Fundamentals and Applications* (2 ed.). Wiley. ISBN 0-471-04372-9.